

THz linear array scanner in application to the real-time imaging and convolutional neural network recognition

A.G. Golenkov, A.V. Shevchik-Shekera, M.Yu. Kovbasa, I.O. Lysiuk, M.V. Vuichyk, S.V. Korinets, S.G. Bunchuk, S.E. Dukhnin, V.P. Reva and F.F. Sizov

V. Lashkaryov Institute of Semiconductor Physics, National Academy of Sciences of Ukraine,
41, prospect Nauky, 03680 Kyiv, Ukraine
E-mail: golenkov@isp.kiev.ua

Abstract. Room temperature linear arrays (up to 160 detectors in array) from silicon metal-oxide-semiconductor field-effect transistors (Si-MOSFETs) have been designed for sub-THz (radiation frequency 140 GHz) close to real-time direct detection operation scanner to be used for detection and recognition of hidden objects. For this scanner, the optical system with aspherical lenses has been designed and manufactured. To estimate the quality of optical system and its resolution, the system modulation transfer function was applied. The scanner can perform real-time imaging with the spatial resolution better than 5 mm at the radiation frequency 140 GHz and contrast 0.5 for the moving object speed up to 200 mm/s and the depth of field 20 mm. The average dynamic range of real time imaging system with 160-detector linear array is close to 35 dB, when the sources with the output radiation power of 23 mW (IMPATT diodes) are used (scan speed 200 mm/s). For the system with 32-detector array, the dynamic range was about 48 dB and for the single-detector system with raster scanning 80 dB with lock-in amplifier. However, in the latter case for obtaining the image with the sizes 20×40 mm and step of 1 mm, the average scanning time close to 15 min is needed. Convolutional neural network was exploited for automatic detection and recognition of hidden items.

Keywords: linear sub-THz array, aspherical optics, scanning systems, convolutional neural network.

<https://doi.org/10.15407/spqeo24.01.090>
PACS 42.79.Ls, 42.79.Pw, 84.35.+i

Manuscript received 12.12.20; revised version received 14.01.21; accepted for publication 10.02.21; published online 09.03.21.

1. Introduction

The spectral range of wavelengths $\lambda \approx 30 \mu\text{m}$ to $\lambda = 3 \text{ mm}$ (radiation frequency $\nu \approx 10 \dots 0.1 \text{ THz}$) is the area for researches that encompass the different spheres of applications. Terahertz (THz) radiation is widely used as a non-destructive evaluation tool for widespread areas. THz technologies are rather hot and important topic, the indicator of which is the number of numerous scientific and engineering researches. They exceed now (together with earlier far-IR papers) the figure of approximately 10000. Out of these applications, a few are in security screening and surveillance, astronomy, spectroscopy, biomedicine, food and package inspection, detection of concealed weapons, vision through camouflage, food testing, etc. (see, e.g., [1-4]). The increasing demand for the fast transmission of large amounts of data will lead to the extension of operation frequencies in communications, toward the THz frequency range. Being non-ionizing in its nature, THz radiation penetrates many dielectric materials like plastics, ceramics, cardboard or dry gypsum plaster-

board (see, e.g., [5-7]) allowing a non-destructive and contact-free testing. At the same time, it is also highly sensitive to water content giving the feasibility to observe the changes of the hydration state of biological matter, e.g., in detecting localization of skin cancer *in vivo*.

2. Considerations

Among different THz technology applications, important are those related with revealing of package inspection and detection of concealed weapons, food and drugs [8-10] as well as development of the methods for automatic detection and identification of hidden items.

Still, in most cases, the THz technologies equipment as a rule is slow and costly and has not yet gained its potential due to complexity of utilization. The necessity of quick and cost-effective non-destructive inspection of hidden or unwanted objects in plastic, cardboard post packages or food containers has been recently grown due to the importance of safety concerns as though promising for a wide range of applying the

THz instrumentation has not yet gained its potential due to a lack of cost-effective, portable, and efficient technologies. To development of the cost-effective instrumentation in these directions, this research is devoted to and based on using uncooled Si-FET detector arrays. Earlier single FET-detectors were applied for getting the images in the sub-THz range [11].

Here, for obtaining the images in close to real-time process in the sub-THz range, Si-FET uncooled multielement linear arrays were used in the developed sub-THz vision system, and a convolutional neural network was exploited for automatic detection and recognition of hidden items. Application of Si complementary metal-oxide semiconductor (CMOS) FETs, SiGe bipolar CMOS, III-V HEMT structures seems applicable, because the respective uncooled detector technology readiness is high [12].

Various techniques can be applied for detection purposes including simple vision inspection, metal and magnetic detectors, X-ray inspection and some others. Among these techniques, different X-ray imaging methods are mostly developed and widely used for revealing the hidden illicit or foreign body items and defects in packed plastic or cardboard mailing envelopes, packages and small containers. However, this technique is well applied for revealing the “hard” items, such as metals, glass or stones and is hardly applied for detection of plastics, dielectrics and, *e.g.*, insects and bugs in dry food products because X-ray transparency of these materials is too high.

There exists a variety of designed THz imaging systems, which have been proposed for non-destructive revealing the concealed objects in post packages or dry food inspection. These systems can be based on time-domain or frequency-domain spectrometers (TDS or FDS) that operate in a wide THz spectral band (see, *e.g.*, [13, 14]), coherent heterodyne or homodyne techniques [15, 16]. Direct detection THz imaging systems based on raster mechanical scanning by using a single detector and monochromatic continuous wave (CW) radiation can be also applied.

All these systems as a rule are time-consuming in obtaining images even at small areas of scanning. *E.g.*, for obtaining images from the area of 10×10 mm with an x - y stepper, it takes 8 min (0.25×0.25 μm pixel) and more when using the TDS method [17]. For larger scanned areas (800×400 mm), it requires the scan time up to 30 min, if using direct detection imaging [18].

Unlike the pulsed THz imaging, presented here CW imaging yields only intensity data and does not provide any depth, frequency-domain or time-domain information about the subject, when a fixed-frequency source and a single detector or arrays of detectors are used. However, the CW imaging systems are sufficient for many imaging applications affording a compact, simple, fast and relatively low-cost system. Since it does not require a pump-probe system and the complexity of the optics involved, the optics of CW systems are much simpler and thus their cost can be considerably reduced as compared to that of the pulsed THz systems [19, 20],

and since it does not require a time delay scan, image formation can proceed quicker [21].

Here, it was designed a THz scanner (Fig. 1) with linear detectors arrays (up to 160 FET detectors) based on CW imaging, which enabled to obtain relatively compact, simple and low-cost system in comparison, *e.g.*, with the TDS approach. This system can operate almost in the real-time domain (with the linear rate up 20 cm/s). Since it does not require a pump-probe laser system and the related optics, this CW system is simpler and costly saving. However, unlike the TDS approach, in this system, the 2D target image is constructed as being based on measurements of the transmitted radiation at a single sub-terahertz or THz frequencies, which is conditioned by the source constant radiation frequency used.

The design of a THz vision system requires reaching the compromise between the resolution, object thickness and cost of THz sources. For the scanner designed, the 140-GHz impact avalanche transit-time (IMPATT) diode sources were mainly used. These sources were applied because of their compact sizes and relatively high output powers and reasonable resolution.

Shown in Fig. 2a are the images of empty lighter and the plain washer at different radiation frequencies $\nu = 140, 96$ and 73.5 GHz, respectively. One can see that at $\nu = 140$ GHz there can be obtained a satisfactory resolution, which allows discerning the items. Moreover, at this radiation frequency, there can be resolved the items with less thickness values (Fig. 2b).

As a rule, for many plastic materials and atmosphere, lower absorption coefficients for 140-GHz radiation as compared to 300 GHz are observed together with much higher radiation output power for IMPATT diodes. The use of sources with a higher output power (clinotron) at $\nu \approx 270$ GHz showed almost the same spectral resolution, but in this case these sources are too

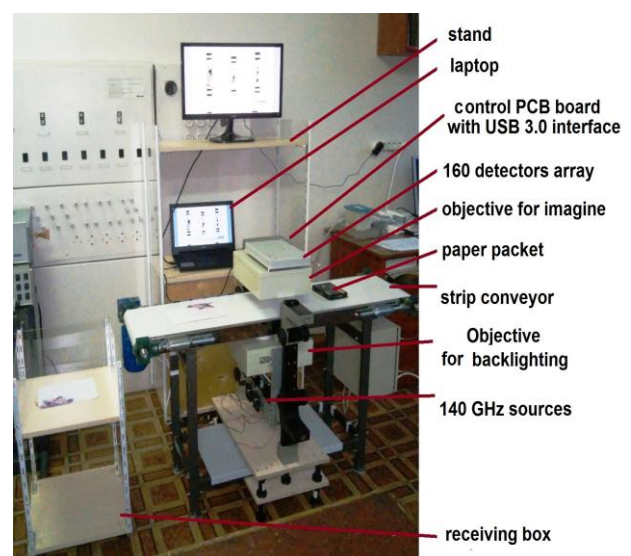


Fig. 1. Photo of the designed THz conveyor type scanner based on 160 Si-MOSFET detectors linear array.

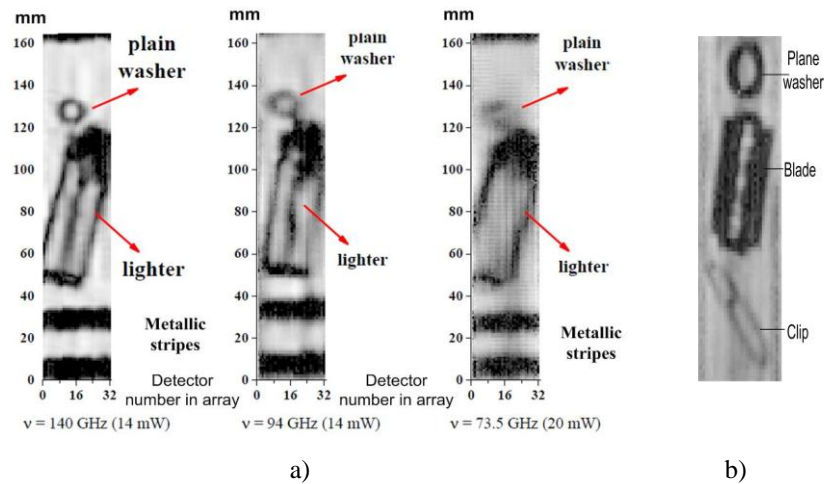


Fig. 2. a) The images of the empty lighter and the plane washer at different radiation frequencies ($\nu = 140, 96$ and 73.5 GHz, respectively) taken with 32-detector linear array. b) The images of a plane washer, blade and a clip at $\nu = 140$ GHz radiation frequency.

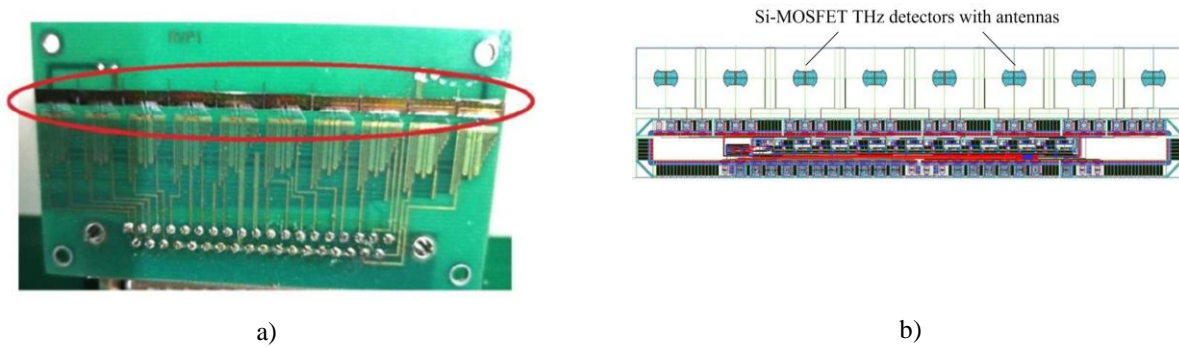


Fig. 3. (a) Eighty Si-MOSFET detectors THz array (emphasized by ellipse) with analog readout on printed circuit board assembled from ten 8-detector linear arrays (b).

bulky and less cost-effective. Moreover, at a lower radiation frequency ($\nu \approx 140$ GHz), the transparency of the refractive optics is higher, and a larger Gaussian beam width provides a greater thickness (because of a larger optic length) of the objects being monitored with an acceptable resolution. In this approach, raster mechanical scanning is not used. Therefore, realization of imaging with the rate close to 200 mm/s can be achieved.

2.1. Si-MOSFET arrays

Here, it was realized the THz conveyor type direct detection imaging system based on the linear antenna-integrated Si-MOSFET detector arrays. Earlier the arrays based on silicon MOSFETs were applied in THz imaging systems (see, *e.g.*, [22, 23]). The known similar systems [24] have a comparable rate of obtaining images but a little bit poorer resolution. The developed here THz image system is simpler than those mentioned above, because of the conveyor type scanning. The use of the linear detector arrays in conjunction with the designed THz objectives made it possible to provide a greater depth of controlled objects in comparison with the known competitive solution for mail scanners [10].

Here, for the THz imaging system we designed the 160-pixel linear arrays comprising 2 or 4 linear arrays of 80 or 40 MOSFET detectors, respectively, with the analog readout. The main components of these assemblies are 8-element integrated linear arrays (Fig. 3). These linear arrays of Si-MOSFET-based direct THz detector were fabricated within the standard $0.35\text{-}\mu\text{m}$ CMOS technology, using three metal levels, ISOMOS (triple well isolated CMOS) transistor as THz detector and poly-silicon capacitors. Each integrated linear array includes 8 pixels with the pitch $V_d = 1$ mm each consisting of on-chip antennas that were connected to the gate and drain of MOSFETs, 8 analog channels for amplification and filtering the output signal, the digital circuit part for scanning signals to one output amplifier and the circuit to control the coefficient of amplification and to generate synchronization signals. The maximum line frequency was 20 kHz and the maximum output signals were about 3 V.

The MOSFET THz detector arrays were designed for using in THz vision system at the radiation frequency close to 280 GHz, but they were used in the scanner operating with the sources of 140 GHz. In this design of the analog channel, there were used two techniques:

the auto-zeroing (AZ) one and correlated double sampling (CDS). The analog channel consists of three stages. The first stage is the differential difference amplifier as the low noise circuit, high gain, auto-zeroing first amplification stage with variable gain; the second stage consists of two differential amplifiers with fixed gain, achieving correlated double sampling; the third stage is the sample and hold stage.

Linear arrays of Si MOSFETs as THz detectors with the pitch 1 mm including antennas, which were initially intended for $\nu \approx 280$ GHz spectral band, were designed. It was shown that these detectors are also applicable for the frequency band 140 GHz, though with less efficiency. The gate-source voltage bias V_{gs} was chosen as $V_{gs} \approx 0.75$ V, where the output signal has its maximum (the threshold voltage was $V_{th} \approx 0.65$ V). Controlling cards connected to linear detector arrays read the signal voltage and transfer to PC information about the radiation power on each Si-MOSFET THz detector. PC software transforms this information into the respective image.

2.2. Optical system, the system modulation transfer function (MTF_{sys}) and system resolution

2.2.1. Optical system

For arrays, the figures of merit for estimations of the vision system performance are the modulation transfer function (MTF) and the phase transfer function (PTF). MTF (defines how the image can be resolved by the system) is one of the primary parameters used in the vision system design, analysis, and specification as a whole, which mostly defines the image quality from the resolution point of view [25, 26]. MTF is the magnitude, and PTF (it determines the image position and orientation, rather than the size of details) is the phase of the complex-valued optical transfer function, which plays a key role in evaluation and optimization of an optical system. For technical vision systems, this complex-valued optical transfer function is maximum at the spatial frequency $f = 1/d$, where d is the extent of one cycle at the target modulation.

To combine an optical resolution and a detector pitch, the function $\lambda F/\# / V_d$ is commonly introduced to characterize the resolution Δ of optical system. Here, $F/\# = fl/D$ is the f -number (focal ratio), fl – effective focal length for thick lenses, λ – average wavelength, and V_d – detector pitch. In the spatial domain, the important parameter is the ratio of the Airy disk diameter to the detector size D_{Airy}/V_d .

For the optical system, the optics with the aspherical lenses were designed and manufactured for the 140-GHz scanner. These lenses have a hyperbolic profile that eliminates the monochromatic aberrations (*e.g.*, spherical aberrations) and leads to an improvement of overall image quality. The objectives from these aspherical lenses are smaller, lighter than the objectives from spherical lenses. They are used to replace several assemblies of spherical elements, which leads to weight loss and to a more compact design. Using the aspherical lenses for THz imaging was discussed, *e.g.*, in [27, 28].

Many plastics are used now for 3D printed THz optics [29], especially in CW systems. Table presents the data for some plastics and other materials, which can be used for manufacturing optical elements for the THz spectral region.

Different approaches to manufacturing the aspherical lenses can be used. In this work, two approaches have been applied for manufacturing the lenses – 3D printing (fused deposition modelling – FDM) and milling, using the CNC (computer numerical control) machining process.

All the materials shown in Table have the slightly frequency-dependent refractive index for applications within the range from 0.2 to 1.4 THz. High impact polystyrene (HIPS) was chosen for manufacturing because it has lower absorption than polyactic acid (PLA), acrylonitrile butadiene styrene (ABS) and tends to be deformed less during printing than high-density polyethylene (HDPE) and polypropylene (PP), nylon.

Here, the CNC machining process has been mainly used for manufacturing the lenses. Teflon with the ultra-high molecular weight and refractive index 1.435 was selected as the lens material for a computer-controlled milling machine. The calculated and experimental diameters of Airy disk of these lenses are close ($D_{Airy-calc} = 7.6$ mm, $D_{Airy-meas} = 8$ mm), which confirms the possibility to produce high-quality aspherical lenses by using the plastic layering method of CNC machining process (Fig. 4). The surface roughness less than approximately $\lambda/20$ was typical for the CNC manufactured Teflon lenses. The diffraction-limited plano-convex aspherical lenses were obtained with the following parameters: the curvature radius of front (+) and rear (–) surfaces was 65 mm; conic constant was $k = -2.6$ (second order surface was hyperboloid), focal length was $fl = 125$ mm for the lenses with $D = 80$ mm. The THz source based on the IMPATT diode with conical horn antenna was used as the emitter generating

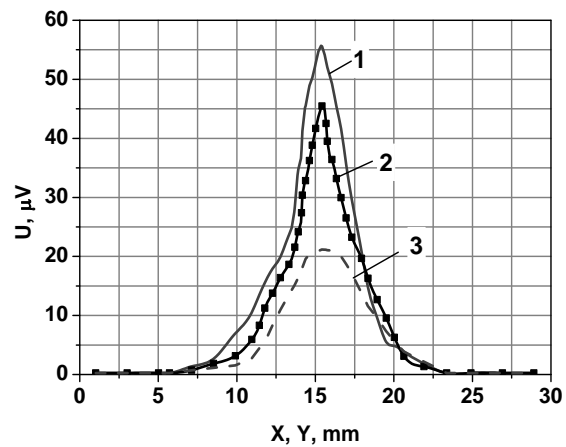


Fig. 4. Distribution of the voltage signal response at the 140-GHz radiation along X and Y axes at the spherical lenses focal plane. The lenses were manufactured using a 3D printer or CNC machining process: 1 – PTFE, 2 – HIPS, 3 – ABS.

Table. Parameters of some materials in THz region ($T = 300$ K) important for THz optics.

Material	Refractive index, n	Absorption coefficient, cm^{-1}	References
ABS	1.57	$\approx 1.5 \dots 25$ (0.2...1.5 THz)	[29]
PLA	1.89	$\approx 1.5 \dots 25$ (0.2...0.9 THz)	[29]
Nylon	1.72	$\approx 0.2 \dots 40$ (0.2...1.2 THz)	[29]
Bendlay	1.53	$\approx 1.5 \dots 25$ (0.5...1.5 THz)	[29]
High impact polystyrene (HIPS)	1.56	$\approx 0 \dots 5$ (0.2...1.5 THz)	[29]
HDPE	1.53	≈ 0 (0.2...1.5 THz)	[29]
PP	1.49	≈ 0.1 (0.2...1.5 THz)	[29]
High-resistance Si	3.42	< 0.05 (0.1...2.0 THz)	[32]
Quartz	1.96	$\approx 1 \dots 9$ (0.1...2.0 THz)	[31]
TPX	≈ 1.45 (0.3...2.5 THz)	0.2...0.9 (0.3...2.5 THz)	[30]
Teflon-AF	≈ 1.39 (0.3...2.5 THz)	$\approx 0.2 \dots 3.4$ (0.3...2.5 THz)	[30]
HDPE	≈ 1.53 (0.3...2.5 THz)	$\approx 0 \dots 2.4$ (0.3...2.5 THz)	[30]
Teflon (PTFE)	≈ 1.435 (0.3...2.5 THz)	$\approx 0 \dots 2.4$ (0.3...2.5 THz)	[30]

ABS is the acrylonitrile butadiene styrene, PLA is the polyactic acid, HDPE is high-density polyethylene, PP is polypropylene, TPX is methyl-pentene copolymer (polymethylpentene), HDPE is the high-density polyethylene, teflon is PTFE (polytetrafluoroethylene).

continuous, linearly polarized, essentially monochromatic radiation with the power $P \approx 20$ mW at the radiation frequency $\nu = 140$ GHz. The radiation from the THz source was focused on the mercury cadmium telluride hot electron bolometer or Si-MOSFET detector.

The distances in the THz optical system designed to items under inspection were small, and attenuation of atmosphere in the radiation frequency range $\nu \sim 40 \dots 300$ GHz was low. Therefore, the influence of atmospheric absorption was here neglected.

Each scanning block scans only a part of the band scanner 160-mm width (the four 40-mm linear arrays of the whole 160-detector linear array). The scanning block consists of a 140-GHz radiation source, condenser, objective and linear detector array. For effective usage of the source power, the condenser provides a linear illumination on the inspected object perpendicular to the scan direction. The condenser forms a uniform radiation flux at the object plane and consists of two aspherical lenses. The first hyperbolic cylindrical lens provides matching between the source and other hyperbolic lenses with account of the angle for beam formation between outgoing radiation from the source horn. To reduce aberrations, two hyperbolic axisymmetrical lenses in objective providing the radiation incidence onto the detector plane were used. The objective focused the transmitted radiation through the inspected object to the linear THz detector arrays. The total transmission coefficient was approximately 63% for condenser (2 lenses) and objective (2 lenses) with 4 aspherical lenses as a whole. For the designed optical system, the depth of field $h \approx 20$ mm was gained allowing to analyze the packages of about 25-mm thickness without distortion and to obtain sufficient sharpness of the images.

2.2.2. System modulation transfer function (MTF_{sys})

The system MTF_{sys} is the characteristic used for the system design and characterization, which takes into account the diameter of the scattering circle (or the Airy disk diameter D_{Airy}), detector dimensions, electronic system, display, etc. and is characterized by the product of optics MTF_{opt} , electronics MTF_{el} , detector MTF_{det} , etc. Here, it is accepted that the MTF of THz system is mainly defined by the product of MTF_{opt} and MTF_{det} , as it is frequently accepted for IR systems. Then for one-dimensional approach along the x -axis (linear array) for any optical system

$$MTF_{sys}(\nu_x) = MTF_{opt}(\nu_x) \times MTF_{det}(\nu_x), \quad (1)$$

where ν_x is the image space frequency (lines pairs per mm) along the x -axis, $MTF_{opt}(\nu_x)$ – MTF of objective, and $MTF_{det}(\nu_x)$ – spatial MTF of a linear array detector.

Space MTF_{det} is the module of normalized Fourier transform of geometrical sizes inherent to the sensitive element. For one-dimensional approach and square law detectors

$$MTF_{det}(\nu_x) = \frac{\sin(\pi \cdot V_d \cdot \nu_x)}{\pi \cdot V_d \cdot \nu_x}. \quad (2)$$

The MTF_{opt} is dependent on the spatial cutoff frequency, which is defined by $\nu_0 = 1/(\lambda \cdot F/\#)$, cycles/mm. The MTF_{opt} for circular aperture with the diffraction limited optics [21] can be represented as

$$MTF_{opt}(\nu_x) = \begin{cases} \frac{2}{\pi} \left(\arccos x - x \sqrt{1-x^2} \right), & \text{at } 0 \leq x \leq 1 \\ 0 & \text{at } x > 1 \end{cases} \quad (3)$$

Here, $x = v_x/v_c$, $v_c = (\lambda \cdot F/\#)^{-1}$ is the cutoff spatial frequency. Image quality is mainly defined by the function $\lambda \cdot F/\# / V_d$.

The deal MTF_{det} is dependent on the detector size, while the diffraction-limited MTF_{opt} is dependent on $F/\#$ and λ . The relationship between the optics and detector can be described by the ratio $\lambda \cdot F/\# / V_d$. This figure of merit can then be used to describe the regions, where a system is described as the diffraction-limited (optics limited) one and is considered as detector-limited [21, 33].

To describe and design IR or THz system operation by spatial resolution and contrast, the MTF_{sys} dependences are usually used, which can be presented as the relationships between the optical MTF_{opt} and the detector MTF_{det} , where the ratio $\lambda(F/\#)/V_d$ is involved.

As $F/\# \cdot (\lambda/V_d)$ decreases, it is going to the regime of detector-limited operation. For operation in the detector-limited region ($F/\# \cdot \lambda/V_d \ll 1$, the detector pitch is much larger than the Airy disk diameter), changing the aperture diameter almost does not influence the spatial resolution.

For large values of $F/\# \cdot \lambda/V_d$, the system becomes optics-limited and the equivalent spatial resolution increases. However, in the optics-limited region ($F/\# \cdot \lambda/V_d \gg 1$), the spatial resolution is poor (the imagery is unclear). Changing the detector pitch in this case does not influence the spatial resolution.

The verge of these approximations can be found from the parity of the diameter of the circle of confusion $2r_{Airy}$ of the optical system and the detector period V_d

$$2.44 \cdot \lambda \cdot F/\# = V_d. \quad (4)$$

From this ratio

$$\frac{\lambda \cdot F/\#}{V_d} = 0.41. \quad (5)$$

In this case, the image resolution is slightly unclear as compared to the detector-limited approximation. According to this condition, there is the valid restriction to match the “objective–detector” system to the detector period. Matching the Airy disk diameter to the detector size (pixel pitch) $D_{dif} = 2.44 \cdot \lambda \cdot F/\# = V_d$. In the optics-limited region, the imagery appears more unclear as compared to the detector-limited one, and smaller detectors have no influence on the system spatial resolution.

When designing the THz imaging system with linear Si-MOSFET arrays, the aim was to get a relatively compact system close to diffraction-limited parameters with low-dimension optics and near to real-time operation. To describe and design the THz system operation by using the spatial resolution and contrast, the MTF_{sys} dependences are usually used, which can be described as relationships between optical MTF_{opt} and detector MTF_{det} , where the ratio $\lambda \cdot (F/\#)/V_d$ is involved, and λ is the radiation wavelength, $F/\#$ - f -number, V_d – detector size. These functions are calculated and shown in Fig. 5 with the parameters $\lambda \approx 2.14$ mm, $V_d = 1$ mm, $F/\# = 1$. Following MTF_{sys} the contrast close to 0.5 is

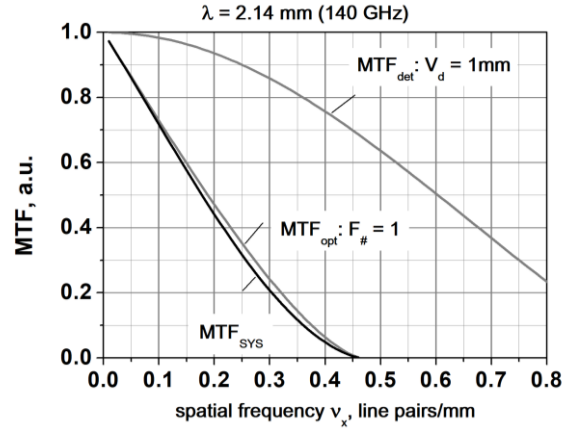


Fig. 5. 140-GHz imaging system MTF_{sys} evaluated dependences for pitch $V_d = 1$ mm and $F/\# = 1$.

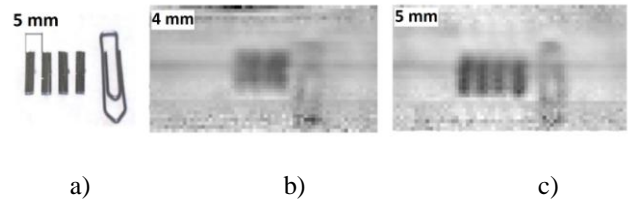


Fig. 6. Visible and 140-GHz images of a metallic pattern for MTF determination: (a) visible photo, (b) 4-mm pattern period ($v_x = 0.25$ mm⁻¹), (c) 5-mm pattern period ($v_x = 0.2$ mm⁻¹). The images were obtained through 5-mm rubber layer for the conveyor strip velocity 200 mm/s.

reached at the spatial frequency 0.2 mm⁻¹, which corresponds to the spatial resolution $\Delta \approx 5$ mm and allows revealing the objects with small dimensions. The designed 140-GHz imaging system provides the spatial resolution $\Delta \approx 5$ mm (see Fig. 6), which is primarily optics-limited.

2.3. Dynamic range

Linear illumination falling onto the inspected object and the focal plane, where the linear arrays are placed, is not uniform along the array axis. Its maximum is located near the centers of the linear arrays, while illumination minimums are located nearer the edges of lines. Thus, if all Si-MOSFET detectors are identical, the voltage signal from each transistor will be different even without any inspected object. Radiation focused onto the Si-MOSFET linear detector arrays falls onto them at different angles of incidence in the center of arrays and at their edges.

That leads to increase in difference between the values of voltage signal, because of the directivity diagram is inherent to antennas. Thus, the dynamic range of sensitive elements depends on the number of elements. Signal-to-noise ratio was measured for all the Si-MOSFET detectors in 32- and 160-element sensitive arrays. In Fig. 7a, one can see that the signal-to-noise ratio is close to the mean value of 48 dB for the array.

The average value of dynamic range of the 160-element sensitive array is close to 35 dB. For illustration of the dynamic range for scanner with 32-detector array, it is seen from Fig. 7b that the razor blade under the rubber sole of thickness $d \approx 4$ mm is clearly seen. For the system with a single THz detector and lock-in amplifier for raster scanning, the dynamic range is $B \approx 80$ dB. However, to obtain the image of sizes 20×40 mm and step of 1 mm, the average scanning time close to 15 min is needed.

The scanner operates in the real-time mode and allows investigating the hidden items in containers and packages made of materials, which are transparent in the THz range with the scan time for 160×240 format image, no long than 1 s (the rate is 200 mm/s). Examples of these materials are plastics, rubber, gypsum plasterboard, ceramics, etc. At the THz frequency $\nu = 140$ GHz, from Fig. 8 one can distinctly see the items under the 12-mm layer of flour.

3. CW THz imaging and convolutional neural network (CNN) for items automatic detection, recognition and identification

Here, the CNN methodology for image recognition from the THz developed scanner was applied. For this application, the architectures from the Tensorflow Object Detection library to an instance segmentation and object detection problems of the concealed items were used.

The convolutional neural networks demonstrate an incredible ability for image recognition in the optical region of spectrum [34]. This is a universal approach that can replace the human ability to detect and recognize objects.

CNN can be used in THz imaging for item recognition or improving resolution. Plenty of libraries and models are available for using this type of neural network. One of the questions is what results will be obtained in the case with one-band low size images. The THz scanner gives one-band speckle records, and it can depend on the sustainability of a model. There is also a challenging question about the size of a dataset that is needed for training self-built and ready pre-trained models. Taking into account all the above, it was settled on an experiment with adaptation of existing models for CNN and choice of the Tensorflow Object Detection [35] as one of the suitable frameworks.

Two main approaches were proposed for detection of concealed items in the images. The first one is an object detection that enables to detect bounding boxes of the detected items, and the other one is an instance segmentation. One of the most successful results on the optical images was shown using the Region-Based Convolutional Networks (RCNN) [36]. We studied several practical realizations of these networks and chose the Tensorflow Object Detection library [35]. For the object detection problem, we picked mobile net CNN that was developed for light-weight applications [37].

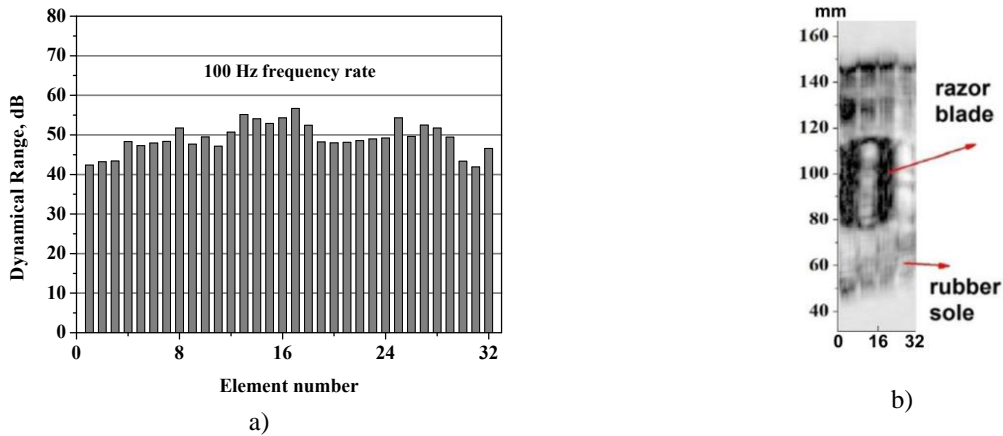


Fig. 7. a) Dynamical range of the THz scanner based on 32-element linear array under 23-mW radiation power of the 140-GHz radiation source. b) The image of the razor blade under the rubber sole (the rubber sole thickness $d \approx 4$ mm), the 140-GHz scanner with the 32-element linear array. The object rate is 200 mm/s.

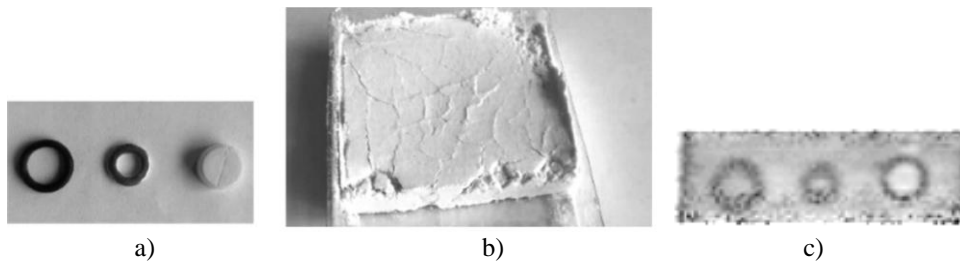


Fig. 8. a) Photo of a rubber washer, a metal washer and a pill in visible light. b) These items under the 12-mm layer of flour in visible light. c) THz image of these items under the 12-mm layer of flour.

The possibility of using CNN in the developed THz scanner for items recognition and identification was tested. The general operational scheme is shown in Fig. 9.

The first stage (Fig. 9) is recording the signals from linear arrays. The developed software (THzView) pre-process acquires and normalizes data. Depending on the chosen mode, THzView prepares images or video as an output. The 160×220 pixels images mode was chosen for the noise reducing and the easily data labelling processes. After that, pictures were rescaled and normalized using the minimum-maximum normalization (see Exp. (6)):

$$I_{output} = (I_{input} - I_{min}) / (I_{max} - I_{min}),$$

$$I_{output} = \text{Log}(I_{input}), \quad (6)$$

where I_{input} is the input image from the scanner; I_{output} – output rescaled image; I_{max} , I_{min} are the global physical maximum and minimum of the signals, respectively.

After acquiring the pictures, the second stage (Fig. 9) is manual annotation of these pictures. The outputs from the Visual Geometry Group annotation tool [38] were proceeded to binary masks of the objects. The third stage is recording the files that are understandable for Tensorflow and then transferring them to laptop deployed software environment for the training stage.

The training stage is fully automated by the Tensorflow Object Detection API free library and was used for convolutional neural network processing. CNN was trained for recognition of plastic cards and lighters with their positions.

The dataset for testing RCNN Inception realization was the set including cards, lighters, knives, packed pills, pills and blades. In total, 1350 images were used for training and 150 for validation. The rule of the same ratio of pictures with different objects in the training and test samples was followed. *E.g.*, 538 images of plastic cards and 525 images of lighter were used to train the developed neural network. 90% of images were used for

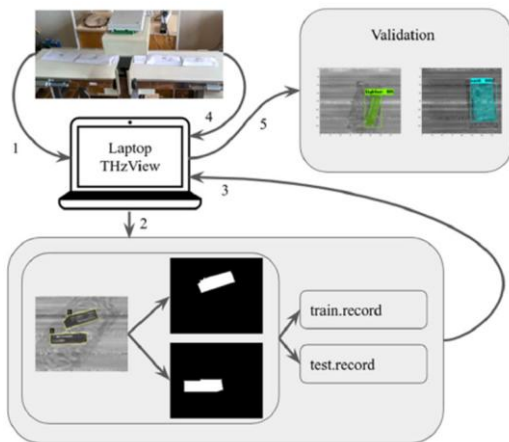


Fig. 9. The general overview of the scheme used for recognition and identification. Numbers near arrows show the main stages.

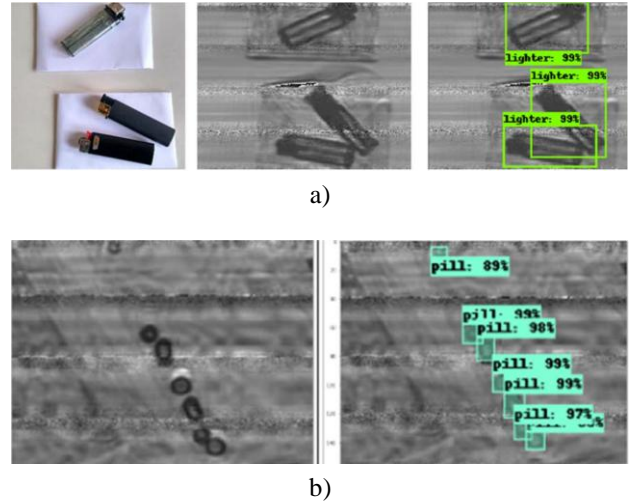


Fig. 10. a) Examples of one and two hidden lighters recognition in envelopes. Photo of lighters are on the left, where these items are located above envelopes for the visibility. b) The results of instance segmentation of hidden 7 pills. The envelopes in which the hidden items are placed could be seen on the background. The values of confidence are shown in the filled rectangles.

training and about 10% of images were used for testing. All items were recognized on the test dataset (*e.g.*, 50 pictures of plastic cards and lighters).

The examples of evaluation of CNN recognition can be seen in Fig. 10, in which there are several types of hidden scanned items. The set of items for recognition can be increased.

4. Conclusions

The active terahertz vision direct detection system has been developed using continuous IMPATT diode radiation sources with the operation frequency 140 GHz ($\lambda = 2.14$ mm) and detector Si-MOSFET linear arrays. Usage of Si-MOSFET arrays reduces the time of scanning the object and supports operation at room temperature.

To increase the spatial resolution of the terahertz vision system and the quality of images, calculation of the modulation transfer function was performed for different cases of matching the parameters of arrays and the optical unit. The terahertz vision system designed with the parameters $\lambda \approx 2.14$ mm, $V_d = 1$ mm, $F/\# = 1$ gives the contrast close to 0.5 at the spatial frequency 0.2 mm^{-1} , which corresponds to spatial resolution $\Delta \approx 5$ mm and enables to reveal the objects with small dimensions.

The possibility of application-ready pre-trained models from the Tensorflow Object Detection library to snapshots from the developed 0.14 THz scanner was demonstrated. With the provided signal-to-noise ratio from 35 to 48 dB from the scanner, the trained models are sustainable and are not influenced by artefacts from the scanner snapshots. The trained RCNN Inception model has shown promising results in the binary experiments with the accuracy close to 97 percents.

Acknowledgments

This research was supported by Ministry of Education and Science of Ukraine within the framework of Project “Terahertz range scanner development for security inspection“. As well as this work was partly supported by the Volkswagen Foundation Partnerships-Cooperation Project No. 97738 “Terahertz optoelectronics in novel low-dimensional narrow-gap semiconductor nanostructures”.

References

1. Fukasawa R. Terahertz imaging: widespread industrial application in non-destructive inspection and chemical analysis. *IEEE Trans. Terahertz Sci. Technol.* 2015. **97**. P. 1121–1127.
2. Mittleman D.M. Twenty years of terahertz imaging. *Opt. Exp.* 2018. **26**. P. 9417–9431. <https://doi.org/10.1364/OE.26.009417>.
3. Martín-Mateos P., Čibiraitė-Lukenskienė D., Barreiro R. *et al.* Hyperspectral terahertz imaging with electro-optic dual combs and a FET-based detector. *Sci. Rept.* 2020. **10**. P. 14429. <https://doi.org/10.1038/s41598-020-71258-6>.
4. Stantchev R.I., Yu X., Blu T., Pickwell-MacPherson E. Real-time terahertz imaging with a single-pixel detector. *Nature Commun.* 2020. **11**. P. 2535. <https://doi.org/10.1038/s41467-020-16370-x>.
5. Hartwick T.S., Hodges D.T., Barker D.H., Foote F.B. Far-infrared imagery. *Appl. Opt.* 1976. **15**. P. 1919–1922. <https://doi.org/10.1364/AO.15.001919>.
6. Gatesman A.J., Danylov A., Goyette T.M. *et al.* Terahertz behavior of optical components and common materials. *Proc. SPIE.* 2006. **2006**. P. 6212. <https://doi.org/10.1117/12.668384>.
7. Busch S., Weidenbach M., Fey M., Schafer F., Probst T., Koch M. Optical properties of 3D printable plastics in the THz regime and their application for 3D printed THz optics. *J. Infrared, Millimeter, Terahertz Waves.* 2014. **35**. P. 993–997. <https://doi.org/10.1007/s10762-014-0113-9>.
8. Davies A.G., Burnett A.D., Fan W., Linfeld E.H., Cunningham J.E. Terahertz spectroscopy of explosives and drugs. *Mater. Today.* 2008. **11**. P. 18–26. [https://doi.org/10.1016/S1369-7021\(08\)70016-6](https://doi.org/10.1016/S1369-7021(08)70016-6).
9. Ok G., Park K., Lim M.-Ch., Jang H.-J., Choi S.-W. 140-GHz subwavelength transmission imaging for foreign body inspection in food products. *J. Food Eng.* 2018. **221**. P. 124–131. <https://doi.org/10.1016/j.jfoodeng.2017.10.011>.
10. Shchepetilnikov A.V., Gusikhin P.A., Muravev V.M. *et al.* New ultra-fast sub-terahertz linear scanner for postal security screening. *J. Infrared, Millimeter, Terahertz Waves.* 2020. **41**. P. 655–664. <https://doi.org/10.1007/s10762-020-00692-4>.
11. Sizov F., Zabudsky V., Golenkov A., Shevchik-Shekera A. Millimeter-wave narrow-gap uncooled hot-carrier detectors for active imaging. *Opt. Eng.* 2013. **52**. P. 033203. <https://doi.org/10.1117/1.OE.52.3.033203>.
12. Sizov F. *Detectors and Sources for THz and IR.* Materials Research Foundations, Vol. 72. Millersville, PA, 2020. <https://doi.org/10.21741/9781644900758>.
13. Neu J., Schmuttenmaer Ch.A. Tutorial: An introduction to terahertz time domain spectroscopy (THz-TDS). *J. Appl. Phys.* 2018. **124**. P. 231101. <https://doi.org/10.1063/1.5047659>.
14. Smolyanskaya O.A., Chernomyrdin N.V., Konovko A.A. *et al.* Terahertz biophotonics as a tool for studies of dielectric and spectral properties of biological tissues and liquids. *Progr. Quant. Electr.* 2018. **62**. P. 1–77. <https://doi.org/10.1016/j.pquantelec.2018.10.001>.
15. Guerboukha H., Nallapan K., Skorobogatiy M. Towards real-time terahertz imaging. *Adv. Opt. Photon.* 2018. **10**. P. 843–937. <https://doi.org/10.1364/AOP.10.000843>.
16. Glaab D., Boppel S., Lisauskas A. *et al.* Terahertz heterodyne detection with silicon field effect transistors. *Appl. Phys. Lett.* 2010. **96**. P. 042106. <https://doi.org/10.1063/1.3292016>.
17. Jokubauskis D., Minkevicius L., Seliuta D., Kasalynas I., Valusis G. Terahertz homodyne spectroscopic imaging of concealed low-absorbing objects. *Opt. Eng.* 2019. **58**. P. 023104. <https://doi.org/10.1117/1.OE.58.2.023104>.
18. Kim K.W., Kim K.-S., Kim H. *et al.* Terahertz dynamic imaging of skin drug absorption. *Opt. Exp.* 2012. **20**. P. 9476–9484. <https://doi.org/10.1364/OE.20.009476>.
19. Kasban H., El-Bendary M.A.M., Salama D.H. A comparative study of medical imaging techniques. *Int. J. Information Sci. Intelligent System.* 2015. **4**, No. 2. P. 37–58.
20. Siebert K., Löffler T., Quast H. *et al.* All-optoelectronic continuous wave THz imaging for biomedical applications. *Phys. Med. Biol.* 2002. **47**. P. 3743–3748.
21. Holst G.C. *Electro-optical Imaging System Performance.* Bellingham, WA, SPIE Optical Eng. Press, 2003.
22. Friederich F., Spiegel W., Bauer M. *et al.* THz active imaging systems with real-time capabilities. *IEEE Trans. Terahertz Sci. Technol.* 2011. **1**. P. 183–200. <https://doi.org/10.1109/TTHZ.2011.2159559>.
23. Triki M., Duhant A., Poulin C. *et al.* Real-time nondestructive imaging with THz waves. *2016 21st Intern. Conf. on Microwave, Radar and Wireless Communications (MIKON)*, Krakow, 2016. P. 1–3. <https://doi.org/10.1109/MIKON.2016.7492135>.
24. Sherry H., Grzyb J., Zhao Y. *et al.* A 1 kpixel CMOS camera chip for 25 fps real-time terahertz imaging applications. *2012 IEEE Intern. Solid-State Circuits Conference.* <https://doi.org/10.1109/ISSCC.2012.6176997>.
25. Holst G.C. *Testing and Evaluation of Infrared Imaging Systems.* Bellingham, WA, SPIE Optical Eng. Press, 1998.

26. Kopeika N.S. *A System Engineering Approach to Imaging*. Bellingham, WA, SPIE Optical Eng. Press, 1998. <https://doi.org/10.1117/3.2265069>.
27. Squires D., Constable E., Lewis R.A. 3D printing of aspherical terahertz lenses and diffraction gratings. *39th Intern. Conference on Infrared, Millimeter, and Terahertz Waves (IRMMW-THz)*, 2014. <http://dx.doi.org/10.1109/IRMMW-THz.2014.6956117>.
28. Lo Y.H., Leonhardt R. Aspheric lenses for terahertz imaging. *Opt. Exp.* 2008. **16**. P. 15991–15998. <https://doi.org/10.1364/OE.16.015991>.
29. Busch S., Weidenbach M., Fey M., Schafer F., Probst T., and Koch M. Optical properties of 3D printable plastics in the THz regime and their application for 3D printed THz optics. *J. Infrared, Millimeter, Terahertz Waves*. 2014. **35**. P. 993–997. <https://doi.org/10.1007/s10762-014-0113-9>.
30. Kawamura J., Paine S., Papa D.C. Spectroscopic measurements of optical elements for submillimeter receivers. *Proc. 7th Intern. Symposium on Space Terahertz Technology*, Charlottesville, 1996. P. 349–355.
31. Naftaly M., Miles R.E. Terahertz time-domain spectroscopy for material characterization. *Proc. IEEE*. 2007. **95**. P. 1658–1665.
32. Grichkowsky D., Keiding S., Van Exter M., Fattinger Ch. Far-infrared time-domain spectroscopy with terahertz beams of dielectric and semiconductors. *J. Opt. Soc. Amer.* 1990. **7**. P. 2006–2015.
33. Holst G.C., Driggers H.G. Small detector in infrared system design. *Opt. Eng.* 2012. **51**. P. 096401. <https://doi.org/10.1117/1.OE.51.9.096401>.
34. McCann M.T., Jin K.H., Unser M. Convolutional neural networks for inverse problems in imaging: A review. *IEEE Signal Processing Mag.* 2017. **34**. P. 85–95. <https://doi.org/10.1109/MSP.2017.2739299>.
35. Huang J., Rathod V., Sun C. *et al.* Speed/accuracy trade-offs for modern convolutional object detectors. *Conference on Computer Vision and Pattern Recognition*, July, 21–26, 2017, Honolulu, HI, USA.
36. Girshick R., Donahue J., Darrell T., Malik J. Region-based convolutional networks for accurate object detection and segmentation. *IEEE Trans. Pattern Analysis Machine Intell.* 2016. **38**. P. 142–158.
37. Howard A.G., Zhu M., Chen B. *et al.* MobileNets: Efficient Convolutional Neural Networks for Mobile Vision Applications. *arXiv:1704.04861 [cs.CV]*. 2017.
38. Dutta A., Zisserman A. The annotation software for images, audio and video. *Proc. 27-th ACM Intern. Conference on Multimedia*. Nice, France, October 21–25, 2019. <https://doi.org/10.1145/3343031.3350535>.

Терагерцовий сканер на основі лінійчатих приймачів випромінювання у застосуванні до систем зору, що працюють в реальному часі, та до розпізнавання за допомогою згорткової нейронної мережі

О.Г. Голенков, А.В. Шевчик-Шекера, М.Ю. Ковбаса, І.О. Лисюк, М.В. Вуйчик, С.В. Корінець, С.В. Бунчук, С.Є. Духнін, В.П. Рева, Ф.Ф. Сизов

Анотація. Лінійчаті приймачі випромінювання (кількість приймачів до 160) на основі кремнієвих метал-оксид-напівпровідникових польових транзисторів (Si-MOH), що працюють при кімнатній температурі, були розроблені для прямого детектування суб-терагерцового (на частоті 140 ГГц) випромінювання в реальному масштабі часу і застосовані в сканері для виявлення та розпізнавання прихованих об'єктів. Для сканера було розроблено та виготовлено оптичну систему з асферичними лінзами. Для оцінки якості оптичної системи та її роздільної здатності застосовано модуляційну передаточну функцію. Сканер може отримувати зображення в режимі реального часу з просторовою роздільною здатністю кращою за 5 мм на частоті 140 ГГц, контрасті ≈ 0.5 , швидкості сканування об'єкта до 200 мм/с та глибини різкості ≈ 20 мм. Середній динамічний діапазон в режимі реального часу розробленої системи зору у випадку лінійчатого 160-елементного приймача складає ≈ 35 дБ при використанні джерела (на основі ІМПАТТ діодів) з потужністю випромінювання ≈ 23 мВт. Для системи, що базується на лінійці з 32 приймачів, динамічний діапазон становив близько 48 дБ, а для системи на основі одноелементного приймача, синхронного детектора та растрового сканування ≈ 80 дБ. Однак в останньому випадку для отримання зображення з розмірами 20×40 мм і кроком сканування 1 мм необхідний середній час ≈ 15 хв. Згорткову нейронну мережу було застосовано для автоматичного виявлення та розпізнавання прихованих елементів.

Ключові слова: лінійчатий суб-ТГц приймач, асферична оптика, скануючі системи, згорткова нейронна мережа.